Editors' Suggestion

Chiral Excitonics in Monolayer Semiconductors on Patterned Dielectrics

Xu-Chen Yang,[1,2] Hongyi Yu,[3] and Wang Yao[1,2,*]
[1]Department of Physics, The University of Hong Kong, Hong Kong, China
[2]HKU-UCAS Joint Institute of Theoretical and Computational Physics at Hong Kong, China
[3]Guangdong Provincial Key Laboratory of Quantum Metrology and Sensing and School of Physics and Astronomy, Sun Yat-Sen University (Zhuhai Campus), Zhuhai 519082, China

(Received 4 September 2021; revised 10 February 2022; accepted 11 April 2022; published 23 May 2022)

Monolayer transition metal dichalcogenides feature tightly bound bright excitons at the degenerate valleys, where electron-hole Coulomb exchange interaction strongly couples the valley pseudospin to the momentum of the exciton. Placed on a periodically structured dielectric substrate, the spatial modulation of the Coulomb interaction leads to the formation of exciton Bloch states with real-space valley pseudospin texture displayed in a mesoscopic supercell. We find this spatial valley texture in the exciton Bloch function is pattern locked to the propagation direction, enabling nano-optical excitation of directional exciton flow through the valley selection rule. The left-right directionality of the injected exciton current is controlled by the circular polarization of excitation, while the angular directionality is controlled by the excitation location, exhibiting a vortex pattern in a supercell. The phenomenon is reminiscent of the chiral light-matter interaction in nanophotonics structures, with the role of the guided electromagnetic wave now replaced by the valley-orbit coupled exciton Bloch wave in a uniform monolayer, which points to new excitonic devices with nonreciprocal functionalities.

DOI: 10.1103/PhysRevLett.128.217402

Chiral quantum optical phenomena have drawn remarkable interest in a variety of optical systems including photonic crystal waveguides [1,2], optical fiber [3,4], whispering-gallery-mode resonators [5,6], plasmonic waveguides [7], and metasurfaces [8]. As light is tightly confined in these nanophotonic structures, its evanescent longitudinal electric field allows a transverse spin (circular polarization) of light with chirality locked to the propagation direction. The combination of such spin-momentum locking of the guided electromagnetic wave with circularly polarized emitters leads to the chiral light-matter interaction [9]. The emitter-photon interplay can become nonreciprocal, i.e., forward- and backward-propagating photons interact differently with the emitter of given polarization, and photon emission can even become unidirectional. The ability to break reciprocity is fundamental for optical devices such as isolators and circulators [10], and enables the construction of complex quantum networks as well as the exploration of radically new quantum many-body phenomena mediated by nonreciprocal channels [9].

Valley exciton in monolayer semiconducting transition metal dicalcogenides (TMDs) has been explored as a new type of polarized emitters for the chiral light-matter interface [7,11]. These monolayer semiconductors feature direct band gaps in visible range [12,13], with band edges at $\mathbf{K}$ and $-\mathbf{K}$ valleys at the Brillouin zone corners. With the strong Coulomb interaction in the 2D geometry, tightly bound Wannier excitons formed in these momentum space valleys dominate the optical responses [14]. Exciton at the $\mathbf{K}$ ($-\mathbf{K}$) valley is interconvertible with a $\sigma+$ ($\sigma-$) polarized photon only [15,16]. Valley polarized excitons prepared by circular optical pumping can therefore be exploited as chiral emitters for coupling to the spin-orbit coupled electromagnetic wave in nanophotonic structures [7,11].

The valley exciton also features a pronounced coupling between its center-of-mass and valley pseudospin degrees of freedom. With small radius, the exciton dispersion at finite momentum is split into a transverse (T) and a longitudinal (L) branch, by the sizable electron-hole Coulomb exchange [14,17–19]. The L (T) branch consists of exciton states with in plane valley pseudospins, that correspond to a linear polarized optical dipole longitudinal (transverse) to exciton momentum [17]. Remarkably, while the T branch has a parabolic dispersion with the regular exciton mass, the L branch is massless with a group velocity proportional to the valley-orbit coupling (Coulomb exchange) strength that is sensitive to surrounding dielectric [14,17–19]. Such a valley-orbit coupled dispersion implies novel control of exciton transport [17], as well as the possibility to tailor exciton dispersions through dielectric engineering [20–23].

Here we show a new type of chiral interface where the role of the spin-orbit coupled electromagnetic wave is now played by the valley-orbit coupled exciton Bloch wave in a uniform monolayer placed on structured dielectric substrate. With the spatial modulation in the valley-orbit coupling strength by the periodic dielectric environment, exciton Bloch bands form where the wave functions feature

spatial texture of valley pseudospin that is pattern locked to the propagation direction. With the mesoscopic periodicity [O(100) nm] of such texture, nano-optical excitation in a selected energy window can directly inject directional exciton flow. The left-right directionality of the exciton current is controlled by the circular polarization of excitation, while the angular directionality is controlled by the excitation location. The current injection rate as a function of the excitation location in a supercell exhibits a vortex (antivortex) pattern for left- (right-) handed circular polarization.

The valley excitons in monolayer TMDs are described by the Hamiltonian $\hat{H} = \sum_{\mathbf{k},\tau}(\hbar^2k^2/2M_0)\hat{B}^\dagger_{\mathbf{k},\tau}\hat{B}_{\mathbf{k},\tau} + \hat{H}_{\rm ex}$, where $\hat{B}^\dagger_{\mathbf{k},\tau}$ creates an exciton with center-of-mass (COM) momentum $\mathbf{k} = (k\cos\theta_{\mathbf{k}}, k\sin\theta_{\mathbf{k}})$ and valley index $\tau = +,-$. The electron-hole exchange $\hat{H}_{\rm ex}$ can be generally expressed as [17] $\hat{H}_{\rm ex} = \sum_{\mathbf{k},\mathbf{k}',\tau,\tau'}\hat{B}^\dagger_{\mathbf{k},\tau}\hat{B}_{\mathbf{k}',\tau'}(\mathbf{k}\cdot\mathbf{d}_\tau)\times(\mathbf{k}'\cdot\mathbf{d}^*_{\tau'})V[\mathbf{k}-\mathbf{k}', (m_h/M_0)\mathbf{k} + (m_e/M_0)\mathbf{k}']$, where $\mathbf{d}_\tau$ is the optical dipole of the exciton which accounts for the wave function overlap between the periodic part of Bloch states in the matrix element of the electron-hole Coulomb exchange. $V(\mathbf{Q},\mathbf{q}) \equiv \int d\mathbf{r}_{\rm eh}d\mathbf{R}\,e^{-i\mathbf{q}\cdot\mathbf{r}_{\rm eh}}e^{-i\mathbf{Q}\cdot\mathbf{R}}V(\mathbf{R},\mathbf{r}_{\rm eh})$ is the Fourier transform of the Coulomb interaction. In the patterned dielectric surrounding, V depends on both the COM coordinate $\mathbf{R} \equiv (m_e/M_0)\mathbf{r}_e + (m_h/M_0)\mathbf{r}_h$, and the electron-hole relative coordinate $\mathbf{r}_{\rm eh} \equiv \mathbf{r}_e - \mathbf{r}_h$ [24,25]. We have dropped the short-ranged part of the exchange which can be regarded as a constant for small values of k and k' [17].

It is convenient to switch to the basis of L and T branch excitons, defined as $\hat{B}^\dagger_{\mathbf{k},L} \equiv (1/\sqrt{2})(e^{-i\theta_{\mathbf{k}}}\hat{B}^\dagger_{\mathbf{k},+} + e^{i\theta_{\mathbf{k}}}\hat{B}^\dagger_{\mathbf{k},-})$ and $\hat{B}^\dagger_{\mathbf{k},T} \equiv (1/\sqrt{2})(e^{-i\theta_{\mathbf{k}}}\hat{B}^\dagger_{\mathbf{k},+} - e^{i\theta_{\mathbf{k}}}\hat{B}^\dagger_{\mathbf{k},-})$. Noting that the exciton has a valley contrasted circularly polarized dipole [15], $\mathbf{d}_\tau = (D/\sqrt{2})(1, -i\tau)$, the exchange term reduces to

$$\hat{H}_{\rm ex} = D^2\sum_{\mathbf{k},\mathbf{k}'}kk'V\left(\mathbf{k}-\mathbf{k}', \frac{m_h}{M_0}\mathbf{k} + \frac{m_e}{M_0}\mathbf{k}'\right)\hat{B}^\dagger_{\mathbf{k},L}\hat{B}_{\mathbf{k}',L} \quad (1)$$

which only affects the L-branch exciton. This conclusion is independent of the form of $V(\mathbf{R},\mathbf{r}_{\rm eh})$. On a homogeneous substrate, the Coulomb interaction depends on $\mathbf{r}_{\rm eh}$ only, so $V(\mathbf{Q},\mathbf{q}) = \delta_{\mathbf{Q},0}(2\pi e^2/\varepsilon q)$. The exciton Hamiltonian becomes $\hat{H} = \sum_{\mathbf{k}}(\hbar^2k^2/2M_0)\hat{B}^\dagger_{\mathbf{k},T}\hat{B}_{\mathbf{k},T} + [(\hbar^2k^2/2M_0) + (2\pi e^2/\varepsilon)D^2k]\hat{B}^\dagger_{\mathbf{k},L}\hat{B}_{\mathbf{k},L}$, i.e., the T branch has the regular exciton mass M_0, while the L branch becomes massless with a group velocity determined by the effective dielectric constant ε [cf. Fig. 1(a)]. We note that *ab initio* calculations have shown a deviation of the L branch from the linear dispersion at large exciton momentum [18,26,27], but the deviation is small in the momentum range concerned. As can be inferred from the discussion below, the linear dispersion is actually not essential, as long as the L branch has a large group velocity and is well separated from the T branch. Also, it has been noted that the electron-hole exchange interaction is not screened by the TMDs layer where exciton resides [18], but can be screened by the dielectric environment [28], the latter responsible for the variation of ε with the change of substrate dielectric.

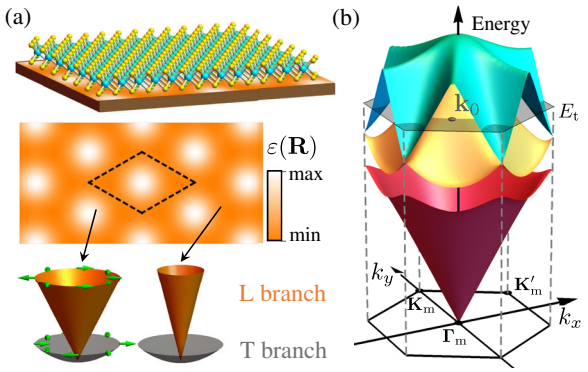

FIG. 1. (a) Schematic of a monolayer TMD on a patterned substrate where the dielectric ε has a triangular superlattice profile as a function of location $\mathbf{R}$. The bottom plots show local dispersions of exciton at the high and low ε regions. Electron-hole Coulomb exchange splits exciton dispersion into L (orange) and T (gray) branches featuring opposite textures of valley pseudospin (green arrows). The L branch has a massless dispersion with velocity $\propto \varepsilon^{-1}$, while the T branch has the usual exciton mass independent of ε. For L branch the modulation $\varepsilon(\mathbf{R})$ leads to the formation of minibands. (b) Typical example of L-branch dispersion shown in the superlattice minizone [the same as Fig. 3(a) where parameters used in the calculation are listed].

Now we consider placing the monolayer on a patterned substrate [Figure 1(a)], where ε gets spatially modulated with a periodicity $l \sim O(100)$ nm. The local dispersion differs from place to place for the L-branch exciton, which leads to the formation of minibands. In the superlattice defined by the patterned dielectric, the Coulomb interaction is of the general form $V(\mathbf{Q},\mathbf{q}) = \sum_{\mathbf{g}}\delta_{\mathbf{g},\mathbf{Q}}V_{\mathbf{g}}(\mathbf{q})$, expanded in terms of the reciprocal lattice vectors $\mathbf{g}$ (cf. Supplemental Material [29]). For smoothly varying ε, keeping the lowest several $\mathbf{g}$ can be sufficient. Equation (1) then becomes $\hat{H}_{\rm ex} = D^2\sum_{\mathbf{k},\mathbf{g}}k|\mathbf{k}+\mathbf{g}|V[\mathbf{g}, \mathbf{k} + (m_h/M_0)\mathbf{g}]\hat{B}^\dagger_{\mathbf{k}+\mathbf{g},L}\hat{B}_{\mathbf{k},L}$. Such momentum scattering of the L-branch exciton by the dielectric superlattice leads to a minigap opening in its dispersion [Fig. 1(b)].

The unfolded L branch features a valley pseudospin texture in momentum space [Fig. 1(a)]. Remarkably, the band folding combined with a momentum-space pseudospin texture in general leads to a superlattice Bloch function with a real-space pseudospin texture in a supercell. Consider, for example, the Bloch function at an arbitrary crystal momentum $\mathbf{k}_0$ in the second lowest miniband [cf. Fig. 1(b)], which has six dominating Fourier components $\hat{B}_{\mathbf{k}_0+\mathbf{g}_i,L}$ with nearly degenerate kinetic energy hybridized by $\hat{H}_{\rm ex}$ [cf. Fig. 2(b)]. Using $\psi^\tau_{\mathbf{k}_0}(\mathbf{R})$ to denote the valley τ component of this Bloch function, the

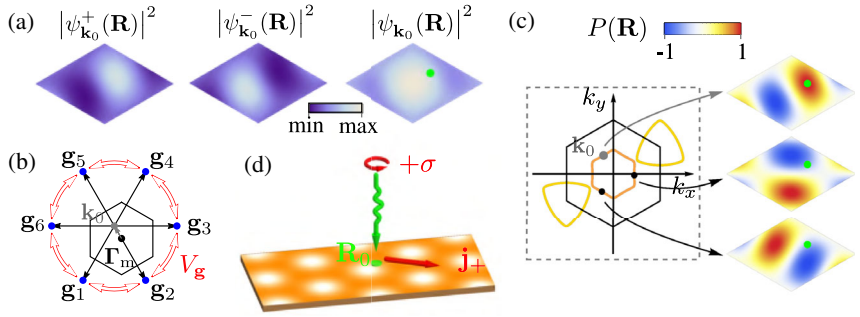

FIG. 2. (a) Example of L exciton Bloch function [at wave vector $\mathbf{k}_0$ denoted by the gray dot in Fig. 1(b)]. Left to right: probability density of the $\mathbf{K}$, $-\mathbf{K}$ valley components, and their sum, shown in a supercell [cf. dashed diamond in Fig. 1(a)]. (b) This Bloch function has six dominant Fourier components at $\mathbf{k}_0 + \mathbf{g}_i$ of the unfolded L branch, which have nearly degenerate kinetic energy, now hybridized by Fourier component $V_\mathbf{g}$ of the electron-hole Coulomb exchange. $\mathbf{g}_i$ are reciprocal superlattice vectors. (c) Spatially resolved valley polarization $P_\mathbf{k}(\mathbf{R})$ in the supercell, shown for three exciton Bloch functions on the contour of energy E_t [cf. Fig. 1(b)]. The orientation of the texture is locked to the superlattice crystal momentum. (d) Through circular polarized nano-optical excitation at $\mathbf{R}_0$, out of the three Bloch states shown in (c), the one at $\mathbf{k}_0$ is selectively excited because of its valley pseudospin texture, leading to a directional exciton flow. Green dots in plots of (a),(c),(d) mark the location of nano-optical excitation.

perturbation expansion leads to (cf. the Supplemental Material [29])

$$|\psi^{\tau}_{\mathbf{k}_0}(\mathbf{R})|^2 = \frac{1}{2} - \frac{g^2\eta}{\mathbf{k}_0\cdot\mathbf{g}_i}\cos\left(\mathbf{g}_i\cdot\mathbf{R} + \tau\frac{\pi}{3}\right) - \frac{g^2\eta}{\mathbf{k}_0\cdot\mathbf{g}_j}\cos\left(\mathbf{g}_j\cdot\mathbf{R} - \tau\frac{\pi}{3}\right), \quad (2)$$

where $\mathbf{g}_i$, $\mathbf{g}_j$ are two reciprocal vectors next nearest to $\mathbf{k}_0$ [i.e., $\mathbf{g}_{4,6}$ in Fig. 2(b)], and η is a dimensionless parameter. Notably, the two valley components $\psi^{+}_{\mathbf{k}_0}(\mathbf{R})$ and $\psi^{-}_{\mathbf{k}_0}(\mathbf{R})$ now display distinct probability distribution, pattern locked to the momentum direction. Figure 2(a) plots the numerically calculated Bloch function for a typical dielectric superlattice, in excellent agreement with Eq. (2). We use $P_\mathbf{k}(\mathbf{R}) = \{[|\psi^{+}_{\mathbf{k}}(\mathbf{R})|^2 - |\psi^{-}_{\mathbf{k}}(\mathbf{R})|^2]/[|\psi^{+}_{\mathbf{k}}(\mathbf{R})|^2 + |\psi^{-}_{\mathbf{k}}(\mathbf{R})|^2]\}$ to quantify the spatial resolved valley polarization. As shown in Fig. 2(c), the spatial pattern of $P_\mathbf{k}(\mathbf{R})$ for the exciton Bloch states rotates with the direction of $\mathbf{k}$.

This makes possible a chiral interface to inject directional exciton flow through a circularly polarized nano-optical excitation [Fig. 2(d)]. Consider an excitation field profile enhanced by a chiral nanostructure [30,31], with a spatial extension of $O(10)$ nm, small compared with the superlattice period l, but orders larger than the monolayer lattice constant (~0.3 nm). The $\sigma+$ polarized optical excitation couples only to the $\tau = +$ valley component of the exciton Bloch state, so the excitation rate is determined by the location-dependent probability density $|\psi^{+}_{\mathbf{k}}(\mathbf{R})|^2$. At given excitation energy, while all $\mathbf{k}$ points on the energy contour can be excited in general, the excitation rate can have a strong dependence on the direction of $\mathbf{k}$, with the angular distribution controlled by the excitation location. For example, among the three Bloch states on the energy contour shown in Fig. 2(c), $\sigma+$ polarized excitation at the green dot will preferentially populate the one at $\mathbf{k}_0$, so the injected excitons correspond to a net flow along the red arrow in Fig. 2(d). The angular directionality is further controlled by the excitation location, evidenced by the $\mathbf{R}$ dependence in Eq. (2) [see also Fig. 2(c)]. Note that momentum conservation is no longer a requirement in the nano-optical excitation with the broken translation symmetry.

For a quantitative analysis of the chiral interface function, we adopt a screened form of the Coulomb interaction $V_\mathbf{g}(\mathbf{q}) = \alpha(\mathbf{g})(2\pi e^2/\varepsilon_c)[1/(\lambda g + q)]$. λg is the screening wave vector (cf. the Supplemental Material [29]), and $\alpha(\mathbf{g})$ is the Fourier coefficient of the spatially modulated dielectric $\varepsilon^{-1}(\mathbf{R}) = \varepsilon_c^{-1}[\alpha(0) + \sum_{i=1}^{6}\alpha(\mathbf{g}_i)\exp(i\mathbf{g}_i\cdot\mathbf{R})]$, the six $\mathbf{g}_i$ shown in Fig. 2(b). Equation (1) then becomes

$$\hat{H}_{\rm ex} = \frac{J}{K}\sum_{\mathbf{k},\mathbf{k}',\mathbf{g}}\delta_{\mathbf{k}',\mathbf{k}+\mathbf{g}}\frac{kk'\alpha(\mathbf{g})}{\lambda g + |\frac{m_h}{M_0}\mathbf{k} + \frac{m_e}{M_0}\mathbf{k}'|}\hat{B}^{\dagger}_{\mathbf{k},L}\hat{B}_{\mathbf{k}',L} \quad (3)$$

where $J \equiv (2\pi e^2 D^2/\varepsilon_c)K \sim 2$ eV can be extracted from first principle wave functions and exciton spectrum [17–19]. We have set the dielectric modulation in a range between $0.9\varepsilon_c$ and $1.3\varepsilon_c$, corresponding to $\alpha(0) = 1$, $\alpha(\mathbf{g}_i) = -0.04$.

Figure 3(a) shows an example of the exciton minibands calculated for $l = 100$ nm and $\lambda = 1$. As expected, only the L branch is affected by the superlattice modulation of the dielectric through the electron-hole exchange interaction $\hat{H}_{\rm ex}$. The spectrum is not sensitive to λ, while the energy scales inversely with l. Examples of the Bloch functions in the second lowest minibands are shown in Figs. 2(a) and 2(c), well described by Eq. (2). Except for the lowest miniband, the pattern locking of the real-space valley texture to the direction of the superlattice crystal momentum $\mathbf{k}$ is generally found. This suggests a large energy window to explore the chiral interface function. The T

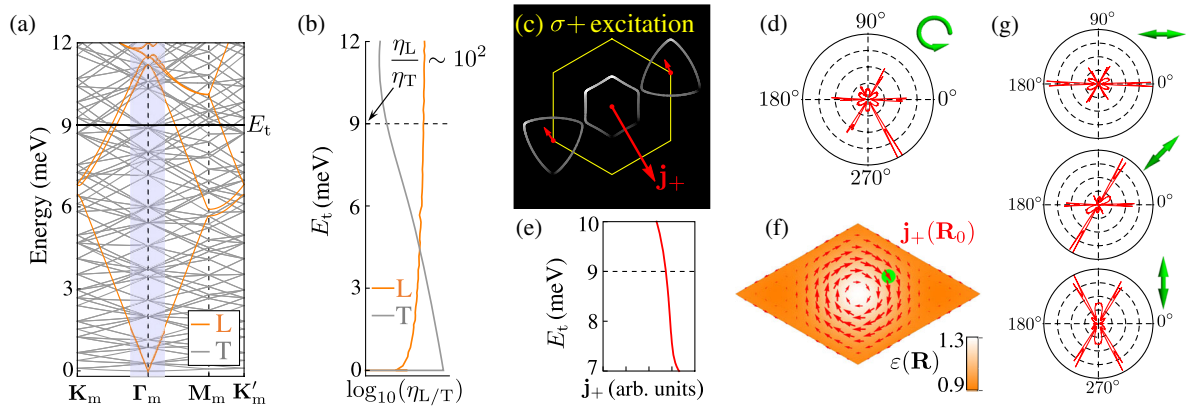

FIG. 3. (a) Exciton dispersion in dielectric superlattice characterized by $\varepsilon^{-1}(\mathbf{R}) = \varepsilon_c^{-1}[\alpha(0) + \sum_{i=1}^{6} \alpha(\mathbf{g}_i)\exp(i\mathbf{g}_i \cdot \mathbf{R})]$, color coded by the projection of the Bloch functions to the T (gray) and L-branch (orange) modes. $\alpha(0) = 1$, $\alpha(\mathbf{g}_i) = -0.04$, corresponding to a dielectric modulation between $0.9\varepsilon_c$ and $1.3\varepsilon_c$. The superlattice period $l = 100$ nm, and electron-hole exchange strength $J = 2$ eV [cf. Eq. (3)]. (b)–(f) Injection of excitons by a $\sigma+$ polarized nano-optical excitation with a field profile $\mathcal{G}(\mathbf{R}) = \exp[-2(\mathbf{R} - \mathbf{R}_0)^2/w^2]$, with $w = 10$ nm centered at $\mathbf{R}_0$. (b) $\eta_{L/T}$ denotes the overall injection rate of L/T excitons as a function of excitation energy E_t. (c) Population distribution of the injected L excitons in momentum space at the excitation energy $E_t = 9$ meV. The anisotropic distribution in momentum space corresponds to an exciton current, primarily contributed by the inner contour (cf. red arrows). (d) Angular distribution of the injected exciton flow. (e) The current injection rate $\mathbf{j}_+$ as a function of E_t. (f) $\mathbf{j}_+$ as a function of excitation location $\mathbf{R}_0$ in a supercell. Green dot marks the excitation location for the plots of (b)–(e). (g) Angular distributions of the injected exciton flow under various linearly polarized excitations at $\mathbf{R}_0$.

branch has more folded minibands in the shown energy range, as its dispersion is much flatter. As the T branch exciton is not affected by the dielectric superlattice, there is no minigap opening.

The excitation rate of an exciton Bloch state is given by $\zeta(\mathbf{k}) = |\langle \psi_{\mathbf{k}}^{+}|\mathcal{G}\rangle|^2$, where $\mathcal{G}$ characterizes the spatial profile of a $\sigma+$ polarized nano-optical excitation. The main results below are insensitive to the detail of $\mathcal{G}$ as long as its spatial extension is small compared with l. For simplicity, we use $\mathcal{G}(\mathbf{R}) = \exp[-2(\mathbf{R} - \mathbf{R}_0)^2/w^2]$, with $w = 10$ nm. Figure 3(b) compares the overall injection rate of L and T branch excitons as a function of excitation energy, $\eta(E_t) = \gamma \int_{E_t}[\zeta(\mathbf{k})/|\nabla_{\mathbf{k}} E|]dk$, where γ is proportional to the field intensity. While the excitation rate of the T branch is higher at the spectral edge because of the larger density of state, starting from the energy window of the second L-branch miniband, the excitation of the L branch dominates, as the T branch modes correspond to large COM momentum that results in diminishing $\zeta(\mathbf{k})$.

Figure 3(c) presents the momentum space distribution of the injected L excitons at $E_t = 9$ meV, where the excitation center $\mathbf{R}_0$ is denoted by the green dot in Fig. 3(f). As expected, a highly anisotropic distribution is injected, which corresponds to a directional exciton flow. Note that these exciton states have a long radiative lifetime as they are outside the light cone, which, combined with their large group velocity, will lead to a long transport length scale. The injection rate of the overall exciton current is

$$\mathbf{j}_+ = \gamma \int_{E_t} \zeta(\mathbf{k}) \frac{\nabla_{\mathbf{k}} E}{|\nabla_{\mathbf{k}} E|} dk. \tag{4}$$

Figure 3(f) plots the current injection rate as a function of the excitation location $\mathbf{R}_0$ in a supercell, which exhibits a vortex pattern. In Fig. 3(g), we also examined the angular directionality upon linearly polarized excitation, where the bidirectional polar distribution is also controllable by the polarization angle. It is worth noting that the shape of the inner energy contour [Fig. 3(c)] has resulted in collimation of the exciton beam along six directions.

The modulated dielectric substrate also introduces superlattice potentials to the electron and hole. In the exciton

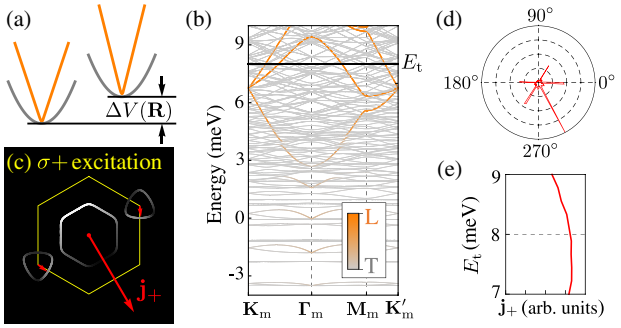

FIG. 4. (a) The patterned dielectric can also lead to a weak spatial modulation of exciton energy $\Delta V(\mathbf{R})$ independent of valley pseudospin. (b) Exciton minibands taking into account $\Delta V(\mathbf{R})$ with a modulation amplitude of 9 meV. Other parameters are the same as in Fig. 3. Above 6 meV, there are minibands predominantly from the L branch (orange). (c) Population distribution of the injected L excitons in momentum space at $E_t = 8$ meV [cf. (a)]. (d) Angular distribution of the injected exciton flow. (e) The current injection rate $\mathbf{j}_+$ as a function of excitation energy E_t.

basis, the superlattice potentials on the electron and hole together correspond to the spatial modulation in the quasiparticle band gap. Exciton energy is the difference of the quasiparticle band gap and the binding energy, both of which are sensitive to the surrounding dielectric [32–34]. For a 1s exciton, nevertheless, various experiments have shown that the optical resonance (dispersion edge) is largely unaffected when the surrounding dielectric varies over a certain range [25,34–36] as the change in band gap and binding energy predominantly cancel each other [37–39]. Experiments in Ref. [25] show that upon the dielectric variation that has resulted in ~30–40% change in exciton binding energy, the change in the 1s exciton optical resonance is only a few meV. This effect can be accounted for by adding a superlattice potential $\Delta V(\mathbf{R})$ independent of valley pseudospin [cf. Fig. 4(a)]. Figure 4(b) plots the exciton minibands, with $\Delta V(\mathbf{R})$ having a modulation amplitude of 9 meV which leads to folding of the T branch, and some hybridization of the L and T branches at low energy. In the spectral window above 6 meV, one can clearly identify minibands arising predominantly from the L branch (orange), where the dispersion largely resembles the ones in the absence of $\Delta V(\mathbf{R})$ [cf. Fig. 3(a)]. Figure 4(c) plots the momentum space distribution of the excitons injected at $E_t = 8$ meV, and Fig. 4(d) shows the angular distribution of the exciton flow. Comparing with the plots of Figs. 3(c) and 3(d), one finds the directionality and the order of magnitude of the exciton current inject remains largely unaffected by $\Delta V(\mathbf{R})$. It is worth noting that the screening effect on the exciton binding can influence the Bohr radius [34] that also determines the strength of the L-T splitting, adding to the dependence of the L-branch group velocity on the surrounding dielectric.

In summary, we show the strong valley-orbit coupling combined with the superlattice modulation leads to a periodic spatial texture of valley pseudospin correlated with the wave vector in exciton Bloch functions. With the mesoscopic superlattice periodicity resolvable in nano-optical excitation, such spatial valley texture can be exploited to realize a chiral interface for the injection of exciton flow. The superlattice modulation naturally arises when the monolayer is placed on a patterned dielectric substrate [21,22], including a photonic crystal slab, where the excitonic and photonic properties can be simultaneously engineered. It is worth noting that such dielectric superlattices have already been demonstrated for graphene using patterned SiO_2 [21,22]. Other candidate substrates include Si_3N_4 and h-BN, which are also exploited for high quality photonic structures [40,41]. A novel alternative for the superlattice modulation of the dielectric surrounding of a monolayer semiconductor was also demonstrated recently using a graphene and h-BN moire superlattice [23]. These point to exciting opportunities toward excitonic devices with nonreciprocal functionalities.

The work is mainly support by the UGC/RGC of Hong Kong SAR (AoE/P-701/20, HKU SRFS2122-7S05), HKU Seed Funding, and Croucher Senior Research Fellowship. H. Y. acknowledges support by the Department of Science and Technology of Guangdong Province in China (2019QN01X061). W. Y. acknowledges support by Tencent Foundation.

*wangyao@hku.hk

[1] I. Söllner, S. Mahmoodian, S. L. Hansen, L. Midolo, A. Javadi, G. Kiršanskė, T. Pregnolato, H. El-Ella, E. H. Lee, J. D. Song *et al.*, Nat. Nanotechnol. **10**, 775 (2015).
[2] B. Le Feber, N. Rotenberg, and L. Kuipers, Nat. Commun. **6**, 6695 (2015).
[3] C. Sayrin, C. Junge, R. Mitsch, B. Albrecht, D. O'Shea, P. Schneeweiss, J. Volz, and A. Rauschenbeutel, Phys. Rev. X **5**, 041036 (2015).
[4] J. Petersen, J. Volz, and A. Rauschenbeutel, Science **346**, 67 (2014).
[5] I. Shomroni, S. Rosenblum, Y. Lovsky, O. Bechler, G. Guendelman, and B. Dayan, Science **345**, 903 (2014).
[6] M. Scheucher, A. Hilico, E. Will, J. Volz, and A. Rauschenbeutel, Science **354**, 1577 (2016).
[7] S.-H. Gong, F. Alpeggiani, B. Sciacca, E. C. Garnett, and L. Kuipers, Science **359**, 443 (2018).
[8] J. Lin, J. B. Mueller, Q. Wang, G. Yuan, N. Antoniou, X.-C. Yuan, and F. Capasso, Science **340**, 331 (2013).
[9] P. Lodahl, S. Mahmoodian, S. Stobbe, A. Rauschenbeutel, P. Schneeweiss, J. Volz, H. Pichler, and P. Zoller, Nature (London) **541**, 473 (2017).
[10] D. Jalas, A. Petrov, M. Eich, W. Freude, S. Fan, Z. Yu, R. Baets, M. Popović, A. Melloni, J. D. Joannopoulos *et al.*, Nat. Photonics **7**, 579 (2013).
[11] Z. Yang, S. Aghaeimeibodi, and E. Waks, Opt. Express **27**, 21367 (2019).
[12] K. F. Mak, C. Lee, J. Hone, J. Shan, and T. F. Heinz, Phys. Rev. Lett. **105**, 136805 (2010).
[13] A. Splendiani, L. Sun, Y. Zhang, T. Li, J. Kim, C.-Y. Chim, G. Galli, and F. Wang, Nano Lett. **10**, 1271 (2010).
[14] H. Yu, X. Cui, X. Xu, and W. Yao, Natl. Sci. Rev. **2**, 57 (2015).
[15] D. Xiao, G.-B. Liu, W. Feng, X. Xu, and W. Yao, Phys. Rev. Lett. **108**, 196802 (2012).
[16] W. Yao, D. Xiao, and Q. Niu, Phys. Rev. B **77**, 235406 (2008).
[17] H. Yu, G.-B. Liu, P. Gong, X. Xu, and W. Yao, Nat. Commun. **5**, 3876 (2014).
[18] D. Y. Qiu, T. Cao, and S. G. Louie, Phys. Rev. Lett. **115**, 176801 (2015).
[19] F. Wu, F. Qu, and A. H. MacDonald, Phys. Rev. B **91**, 075310 (2015).
[20] M. I. B. Utama, H. Kleemann, W. Zhao, C. S. Ong, H. Felipe, D. Y. Qiu, H. Cai, H. Li, R. Kou, S. Zhao *et al.*, National electronics review **2**, 60 (2019).
[21] C. Forsythe, X. Zhou, K. Watanabe, T. Taniguchi, A. Pasupathy, P. Moon, M. Koshino, P. Kim, and C. R. Dean, Nat. Nanotechnol. **13**, 566 (2018).

[22] Y. Li, S. Dietrich, C. Forsythe, T. Taniguchi, K. Watanabe, P. Moon, and C. R. Dean, Nat. Nanotechnol. **16**, 525 (2021).
[23] Y. Xu, C. Horn, J. Zhu, Y. Tang, L. Ma, L. Li, S. Liu, K. Watanabe, T. Taniguchi, J. C. Hone *et al.*, Nat. Mater. **20**, 645 (2021).
[24] A. Chernikov, T. C. Berkelbach, H. M. Hill, A. Rigosi, Y. Li, O. B. Aslan, D. R. Reichman, M. S. Hybertsen, and T. F. Heinz, Phys. Rev. Lett. **113**, 076802 (2014).
[25] A. Raja, L. Waldecker, J. Zipfel, Y. Cho, S. Brem, J. D. Ziegler, M. Kulig, T. Taniguchi, K. Watanabe, E. Malic *et al.*, Nat. Nanotechnol. **14**, 832 (2019).
[26] T. Deilmann and K. S. Thygesen, 2D Mater. **6**, 035003 (2019).
[27] D. Y. Qiu, G. Cohen, D. Novichkova, and S. Refaely-Abramson, Nano Lett. **21**, 7644 (2021).
[28] D. Y. Qiu, F. H. da Jornada, and S. G. Louie, Phys. Rev. B **103**, 045117 (2021).
[29] See Supplemental Material at http://link.aps.org/supplemental/10.1103/PhysRevLett.128.217402 for detailed analysis to the Coulomb exchange interaction and the Bloch function of the exciton in monolayer TMDs on patterned dielectric.
[30] M. Qiu, L. Zhang, Z. Tang, W. Jin, C.-W. Qiu, and D. Y. Lei, Adv. Funct. Mater. **28**, 1803147 (2018).
[31] H. Gao, P.-G. Chen, T. W. Lo, W. Jin, and D. Lei, Adv. Funct. Mater. **31**, 2101502 (2021).
[32] M. M. Ugeda, A. J. Bradley, S.-F. Shi, F. H. da Jornada, Y. Zhang, D. Y. Qiu, W. Ruan, S.-K. Mo, Z. Hussain, Z.-X. Shen, F. Wang, S. G. Louie, and M. F. Crommie, Nat. Mater. **13**, 1091 (2014).
[33] A. Raja, A. Chaves, J. Yu, G. Arefe, H. M. Hill, A. F. Rigosi, T. C. Berkelbach, P. Nagler, C. Schüller, T. Korn, C. Nuckolls, J. Hone, L. E. Brus, T. F. Heinz, D. R. Reichman, and A. Chernikov, Nat. Commun. **8**, 15251 (2017).
[34] A. V. Stier, N. P. Wilson, G. Clark, X. Xu, and S. A. Crooker, Nano Lett. **16**, 7054 (2016).
[35] Y. Xu, S. Liu, D. A. Rhodes, K. Watanabe, T. Taniguchi, J. Hone, V. Elser, K. F. Mak, and J. Shan, Nature (London) **587**, 214 (2020).
[36] Y. Lin, X. Ling, L. Yu, S. Huang, A. L. Hsu, Y.-H. Lee, J. Kong, M. S. Dresselhaus, and T. Palacios, Nano Lett. **14**, 5569 (2014).
[37] D. Y. Qiu, F. H. da Jornada, and S. G. Louie, Phys. Rev. Lett. **111**, 216805 (2013).
[38] Y. Cho and T. C. Berkelbach, Phys. Rev. B **97**, 041409(R) (2018).
[39] S. Gao, Y. Liang, C. D. Spataru, and L. Yang, Nano Lett. **16**, 5568 (2016).
[40] C. Qian, V. Villafañe, P. Soubelet, A. Hötger, T. Taniguchi, K. Watanabe, N. P. Wilson, A. V. Stier, A. W. Holleitner, and J. J. Finley, arXiv:2107.04387.
[41] J. E. Fröch, L. P. Spencer, M. Kianinia, D. D. Totonjian, M. Nguyen, A. Gottscholl, V. Dyakonov, M. Toth, S. Kim, and I. Aharonovich, Nano Lett. **21**, 6549 (2021).